Article

First-Principles Study of Optoelectronic Properties of the Noble Metal (Ag and Pd) Doped BiOX (X = F, Cl, Br, and I) Photocatalytic System

Shixiong Zhou [1,2]**, Tingting Shi** [3,*]**, Zhihong Chen** [4]**, Dmitri S. Kilin** [5]**, Lingling Shui** [1]**, Mingliang Jin** [1]**, Zichuan Yi** [2]**, Mingzhe Yuan** [4]**, Nan Li** [2]**, Xiaobao Yang** [6]**, Qingguo Meng** [4,5,*]**, Xin Wang** [1,*] **and Guofu Zhou** [1,2]

[1] National Center for International Research on Green Optoelectronics, South China Academy of Advanced Optoelectronics, South China Normal University, Guangzhou 510006, China; shixiong.zhou@ecs-scnu.org (S.Z.); shuill@m.scnu.edu.cn (L.S.); jinml@scnu.edu.cn (M.J.); guofu.zhou@m.scnu.edu.cn (G.Z.)

[2] Shenzhen Guohua Optoelectronics Tech. Co. Ltd., Shenzhen 518110, China; zichuan.yi@guohua-oet.com (Z.Y.); nan.li@guohua-oet.com (N.L.)

[3] Siyuan Laboratory, Guangzhou Key Laboratory of Vacuum Coating Technologies and New Energy Materials, Department of Physics, Jinan University, Guangzhou 510632, China

[4] Shenyang Institute of Automation, Guangzhou, Chinese Academy of Sciences, Guangzhou 511458, China; chenzhihong1227@sina.com (Z.C.); mzyuan@sia.cn (M.Y.)

[5] Department of Chemistry and Biochemistry, North Dakota State University, Fargo, ND 58108, USA; dmitri.kilin@ndsu.edu

[6] Department of Physics, South China University of Technology, Guangzhou 510640, China; scxbyang@scut.edu.cn

* Correspondence: ttshi@jnu.edu.cn (T.S.); mengqingguo@gz.sia.cn (Q.M.); wangxin@scnu.edu.cn (X.W.)

Abstract: To explore the photocatalytic performances and optoelectronic properties of pure and doped bismuth oxyhalides D-doped BiOX (D = Ag, Pd; X = F, Cl, Br, I) compounds, their atomic properties, electronic structures, and optical properties were systematically investigated using first-principles calculations. In previous experiments, the BiOX (X = Cl, Br) based system has been observed with enhanced visible light photocatalytic activity driven by the Ag dopant. Our calculations also show that the potential photocatalytic performance of Ag-doped BiOCl or BiOBr systems is enhanced greatly under visible light, compared with other Pd-doped BiOX (X = Cl, Br) compounds. Furthermore, it is intriguing to find that the Pd-doped BiOF compound has strong absorption over the infrared and visible light spectrum, which may offer an effective strategy for a promising full spectrum catalyst. Indicated by various Mulliken charge distributions and different impurity states in the gap when Ag or Pd was doped in the BiOX compounds, we notice that all D-doped BiOXs exhibit a p-type semiconductor, and all impurity levels originated from the D-4d state. The charge transfer, optoelectronic properties, and absorption coefficients for photocatalytic activities among D-doped BiOX photocatalysts caused by the electronegativity difference of halide elements and metal atoms will finally affect the photocatalytic activity of doped BiOX systems. Therefore, it is significant to understand the inside physical mechanism of the enhanced Ag/Pd-doped BiOX photocatalysts through density functional theory.

Keywords: photocatalytic performance; metal doping; electronic structure; optical absorption; first-principles

1. Introduction

The shortage of energy resources and the pollution of environments in the world have become hot topics nowadays. Since Fujishima discovered the phenomenon of water decomposed by TiO_2 photocatalysts under light [1], photocatalysts-based semiconductors have attracted extensive attention for developing new energy resources and eliminating pollutants [2,3]. This includes, for example, oxygen evolution, hydrogen evolution, CO_2 reduction, nitrogen fixation, organic syntheses, disinfection, and organic pollutant removal [4–6]. However, the catalytic efficiency of TiO_2 is too low for commercial technology. The main detrimental drawbacks are the rapid recombination of photo-generated electron/hole pairs and the backward reaction and poor activation of TiO_2 by visible light [7,8]. Large numbers of novel photocatalytic materials are studied [9–14], especially BiOX (X = F, Cl, Br and I) compounds because of their high photocatalytic performance. Since the better performance of BiOCl over TiO_2 at three cycles on the photocatalytic degradation of methyl orange (MO) dye was observed by Zhang et al. in 2006 [15,16], a series of novel Bismuth oxyhalides (BiOX, X = Cl, Br, and I) photocatalysts were synthesized by employing ethylene glycol as the solvent [17], which displayed the outstanding photocatalytic performances under UV-Vis light irradiation. Meanwhile, the theoretical calculations were also employed to investigate the physical mechanism of BiOX photocatalysts. Due to the unique stack-layered structural properties of BiOX compounds, its photocatalytic efficiency can be tuned feasibly by controlling the intensity of the electrical field. The investigation of structural and optoelectronic properties of BiOX is the threshold to clarifying the photocatalytic activity. Huang et al. calculated the electronic and optical properties of the BiOX with and without the adoption of Bi-5d state and they showed that all BiOX are indirect band-gap materials, except the direct band-gap BiOF compound [18]. The incorporation of the Bi-5d state, the Bi-5f state, and the correction of van der Walls (vdW) in the calculations did not largely change the band characteristics, but only enlarged the band gap slightly [19,20].

However, the photocatalytic activities of BiOCl under visible light are insufficient due to a large band gap, and the redox reaction of BiOI is weak because of its higher valence band edge [21–23], so for the band engineering process through interface design, impurity doping can be employed to make up for the deficiencies.

Many studies have been further attempted to reinforce the photocatalytic activity of BiOX systems, such as heterostructure designs of BiOBr/AgBr, $BiOCl/BiO_3$, BiOBr/BiOI [24–29] and some specific impurity doping [30–33]. Dai et al. proved that the photoluminescence, photocatalytic activity, and strong optical properties of Eu^{3+}-doped BiOX (X = F, Cl, Br, and I) could be enhanced using the density functional theory (DFT) method [30]. Zhao et al. explored the catalytic mechanism of $BiOX_{1-r}Y_r$ (X, Y = F, Cl, Br, I, 0 < r < 1) from the perspective of lattice constants, band gaps, and optical properties, and the results showed that the optical properties linearly vary as a function of the r-value and the band gap of $BiOX_{1-r}Y_r$ solid solutions can be tuned from 1.7–4.0 eV by changing the halogen composition [31]. Also, the co-doping of Sb and I atoms in BiOCl can obviously decrease the band gaps and increase the optical absorption coefficients [28]. In Yu's experiments, transition metals, such as Ag, Pd, Pt, and Rh are also important dopants which could be considered to enhance the optical properties and photocatalytic performance of BiOX (X = Cl, Br, and I) [32,33]. It was reported that the Ag-doped BiOX-based system had higher VLD (visible-light-driven) photocatalytic activity due to the degradation of rhodamine B [34]. Other ternary heterojunction compounds $Ag/AgBr/BiOIO_3$ are synthesized which show strengthened photocatalytic activity owing to the Ag doping [35]. Kim group synthesized the Ag and Au doped $BiOCl/BiOCl_xI_{1-x}$ compounds and proved that the light absorption and photocatalytic activity of these samples were improved [36].

There are a series of experimental investigations of transition metal doped BiOX photocatalysts, but the theoretical investigation of these transitional metal doped BiOX compounds remains insufficient. Since there are few computational calculations reported regarding Ag and Pd doped BiOCl, BiOBr, BiOI, and BiOF photocatalysts, in this work we systematically focus on the structural, electronic, and optical properties of pure and D-doped BiOX (D = Ag and Pd) models using the density functional theory

(DFT) calculations. From the variation of the charge distribution and optical spectrum before and after doping Ag/Pd in the BiOX system, the mechanisms of their enhanced photocatalyst performances were interpreted.

2. Theoretical Method

2.1. Computational Models

The BiOX (X = F, Cl, Br, and I) compounds posess a tetragonal structure with the space group of P4/nmm (NO. 129) [37,38]. The primitive cell contains 6 atoms and the lattice parameters are given as follows: a = b = 3.756 Å, c = 6.234 Å for BiOF [37]; a = b = 3.890 Å, c = 7.370 Å for BiOCl [37,38]; a = b = 3.920 Å, c = 8.110 Å for BiOBr [37,38], a = b = 4.090 Å, c = 7.210 Å for BiOI [37,38], and the angles are α = β = 90°. In the present work, a 3 × 3 × 2 supercell model and transitional metal doped models were constructed as shown in Figure 1. One Bi atom was displaced by a metal atom as substitutional doping, shown as Figure 1b. In the supercell, the number of atoms is 108, and the metal doping concentration is 0.926% (atom fraction). The 3 × 3 × 2 supercell was adopted to avoid impurity and self-interaction. The structure surrounding impurity atom D is illustrated as Figure 1c. The bond length d_i (*i* = 1, 2, 3, and 4) and angle α_j (*j* = 1 and 2) of the D-related location were calculated.
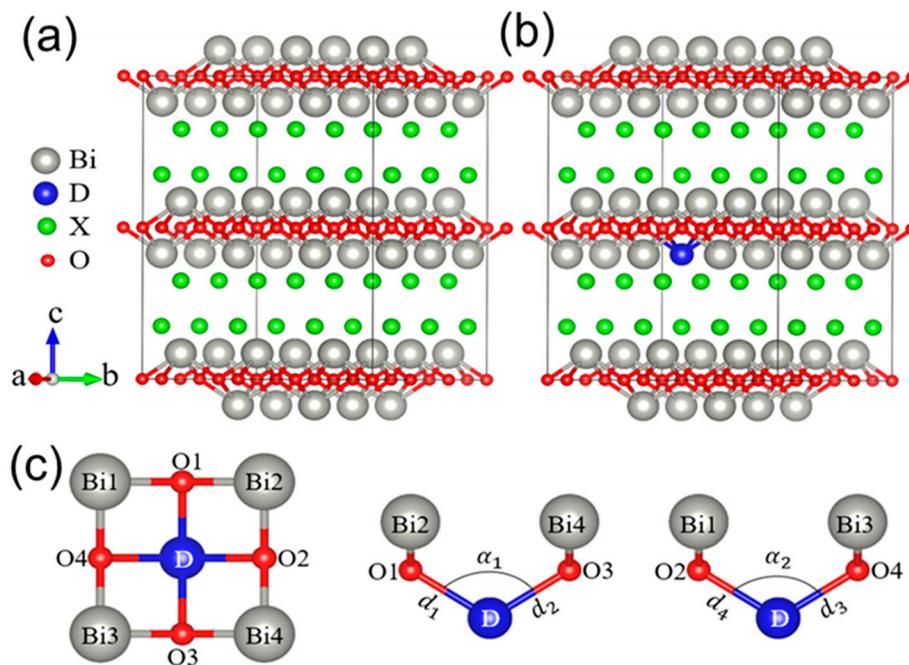

Figure 1. The (**a**) pure and (**b**) D-doped BiOX model. In figure (**c**), d_i (*i* = 1, 2, 3, 4) is the bond length for O1-Ag, O3-Ag, O2-Ag, and O4-Ag respectively; α_j (*j* = 1, 2) is the bond angle for O1-Ag-O3 and O2-Ag-O4, respectively. A Bi atom is replaced by a metal atom, signed D. The atom numbers of the BiOX supercell are 108, and that is (BiOX)36. The stoichiometric ratio of the different species of doping models, Bi:O:X:D, is 35:36:36:1.

2.2. Computational Methods

In this work, all calculations were conducted via the well-tested Cambridge Serial Total Energy Package (CASTEP, http://www.castep.org/) codes based on density functional theory (DFT) [39]. The exchange-correlation potential was described with the generalized gradient approximation (GGA) in the scheme of Perdew-Burke-Ernzerh for solids (PBEsol) [40]. The Kohn-Sham wave functions of valence electrons (Bi$6s^26p^3$, O$2s^22p^4$, F$2s^22p^5$, Cl$3s^23p^5$, Br$4s^24p^5$, I$5s^25p^5$, Ag$4d^{10}5s^1$, Pd$4d^{10}$) were expanded in a plane-wave within the cutoff energy of 430 eV. The Brillouin Zone was sampled with a 2 × 2 × 1 k-point grid for a supercell using the Monkhorst Pack scheme [41]. More k points

$3 \times 3 \times 2$ were tested and the results changed very little. The spin was considered as the input file and the dipole moment was equal to zero, which is verified by taking the Ag-doped BiOBr model as an example, as shown in Figure S1 of the Supplementary Information (SI). A $60 \times 60 \times 90$ mesh was used for the Fast Fourier Transformation (FFT). The Broyden−Fletcher−Goldfarb−Shanno (BFGS) scheme was chosen as the minimization algorithm [42]. Its convergence standards were set as the follows: the force on the atoms was less than 0.05 eV/Å; the stress on the atoms was less than 0.1 Gpa; the maximum atomic displacement was less than 0.002 Å, and the energy change per atom was less than 2×10^{-5} eV. On the basis of optimized crystalline structures, electronic structures and optical properties were computed. From the band structure to the density of states, Gaussian broadening is applied to the eigenvalues, and smearing width is set as 0.1 eV. Meanwhile, the self-consistent field (SCF) tolerance was 1×10^{-6} eV. In addition, the high symmetry points for band structure calculation are $\Gamma(0.00, 0.00, 0.00) \rightarrow F(0.00, 0.50, 0.00) \rightarrow Q(0.00, 0.50, 0.50) \rightarrow Z(0.00, 0.00, 0.50)$ in k-space.

2.3. The Formula of Absorption Coefficients

The optical properties were calculated based on the crystalline and electronic structure by the first principle, which was obtained from the frequency-dependent complex dielectric function $\varepsilon(\omega) = \varepsilon_1(\omega) + i\varepsilon_2(\omega)$ following a methodology described in the literature [43]. The real part $\varepsilon_1(\omega)$ is obtained using the Kramers-Kronig relation, and it is defined as the electronic contribution to the dielectric constant, whereas the imaginary part $\varepsilon_2(\omega)$ was calculated by the sum of all possible transitions from occupied to unoccupied states in the Brillouin zone weighted with the matrix elements describing the probability of transition. To determine the fraction of the light absorbed in these materials, the absorption coefficients $\alpha(\omega)$ (in cm^{-1}) were calculated for each compound as the function of the wavelength of incident light using the following equations:

$$\alpha(\omega) = \frac{4\pi k(\omega)}{\lambda} \tag{1}$$

$$k(\omega) = \left(\frac{\sqrt{\varepsilon_1^2 + \varepsilon_2^2} - \varepsilon_1}{2} \right)^{\frac{1}{2}} \tag{2}$$

where λ and ω are the wavelength and frequency of the incident light, respectively, and $k(\omega)$ represents the extinction coefficient. The relationship between energy in eV and wavelength in nm is:

$$E(eV) = \frac{1240}{\lambda} \tag{3}$$

3. Results and Discussion

3.1. Structural Optimization

The structure of the pure and Ag and Pd doped BiOX models were optimized respectively under the same conditions in order to reduce system error. Lattice constants of the pure unit cells of the BiOX (X = F, Cl, Br, and I) compounds were stabilized as a = b = 3.732, c = 6.158 for BiOF, a = b = 3.875, c = 7.367 for BiOCl, a = b = 3.900, c = 8.304 for BiOBr, a = b = 3.972, c = 9.318 for BiOI (in Å), in agreement with the experimental data [37].

The variation of lattice parameters of the Ag and Pd doped BiOX models after optimization (parameter difference before and after optimization), such as average variation of bond length Δd, bond angle $\Delta \alpha$, and lattice constant Δa are listed in Table 1, and details in Table S1 to evaluate the effect of the doped metal atoms on the lattice structure of the BiOX models. The results indicate that some changes of bond length and angel are attributed to the difference of valence electrons of Ag, Pd, and Bi, and the electronegativity of halogen atoms. However, the BiOX compounds still remain as layered structures, so the internal electronic field still plays a positive role in carries separation.

Table 1. The variation of structural parameters (parameter difference before and after optimization), bond length of Bi-O *L*, band gaps E_g, and absorption edge *Abs*. Δa are variation of lattice constant *a*; Δd is bond length variation, $\Delta\alpha$ is bond angle variation, and E_{for} is the formation energy of the doping system.

	Δa/Å	$\frac{\Delta d}{\text{Å}}$	$\frac{\Delta\alpha}{\text{Å}}$	*L* */Å	E_{for}/eV	E_g/eV	*Abs*/nm
BiOF	-	-	-	2.278 [a] 2.275	-	4.553 [b] 3.193	286
Ag/BiOF	0.061	−0.277	45.036	1.998	−8.12	3.101	551
Pd/BiOF	0.060	−0.302	44.808	1.973	−5.95	2.905	>780
BiOCl	-	-	-	2.314 [a] 2.315	-	3.44 [b]/2.50 [c] 2.483	355
Ag/BiOCl	−0.015	−0.269	40.275	2.046	−8.06	2.569	650
Pd/BiOCl	−0.002	−0.296	50.827	2.019	−5.95	2.437	559
BiOBr	-	-	-	2.320 [a] 2.322	-	2.91 [b]/2.10 [c] 2.098	451
Ag/BiOBr	−0.016	−0.276	40.275	2.046	−8.07	2.280	696
Pd/BiOBr	−0.012	−0.299	47.219	2.023	−5.95	2.152	479
BiOI	-	-	-	2.329 [a] 2.324	-	1.92 [b]/1.59 [c] 1.513	650
Ag/BiOI	−0.013	0.194	−7.451	2.518	−8.06	1.504	844
Pd/BiOI	−0.012	−0.233	46.415	2.091	−5.96	1.558	759

[a] Zhang et al. Phys Chem Chem Phys, 2014, 16, 25854–25861; [b] Wu et al. 2016 IEEE International Conference on EIT, Grand Forks, ND, 2016, 0452–0457; [c] Zhao et al. Physica B: Condensed Matter, 2012, 407, 3364–3370; * Bond length of Bi-O values are the D-O's after doping for the D/BiOX (D = Ag and Pd).

The formation energy is a typical physics parameter that explains the formation of the crystal from isolated atoms. In this work, the formation energy is defined as:

$$E_{for} = E_{D/BiOX} - E_{BiOX} - \mu_D + \mu_{Bi} \qquad (4)$$

according to Van de Walle [44], where E_{for} is the average formation energy of the systems, $E_{D/BiOX}$ and E_{BiOX} are the total energies of the D-doped BiOX and pure BiOX, respectively, and μ_D and μ_{Bi} are the chemical potentials for Ag (or Pd) and Bi, respectively. The more negative value of E_{for} indicates a more stable substance. The calculated formation energy values of all doped BiOX models are listed in Table 1. As we can see, all the doped structures are stable, and the Ag-doped BiOX structures are more stable than the Pd doped models.

3.2. Electronic Structures

The band structures of the pure and D-doped BiOX models are computed and the results are listed in Table 1. The Fermi energy level is set at the valence band maximum. First, we discuss the pure BiOX compounds. The band gap of the BiOF model is 3.193 eV, whose valence band maximum (VBM) and conduction band minimum (CBM) are at the k-point of Γ from the Figure S2, indicating a direct semiconductor. The band gaps of BiOX (X = Cl, Br, I) are 2.483, 2.098, and 1.513 eV, respectively. These BiOX models are indirect semiconductors. All of the band gaps of BiOX are lower than the experimental value, which is caused by the well-known inherent shortcomings of the GGA functional. However, the variation trend of the band gap is consistent with the experimental results as E_g(BiOF) > E_g(BiOCl) > E_g(BiOBr) > E_g(BiOI) [17–20], which decreases with the increase of the halogen atomic numbers. Moreover, the indirect semiconductor can prevent electron-hole pair recombination. A small band gap could facilitate the excitation of electrons from the top of the valence band to the bottom of conduction band, requiring less light energy.

Secondly, as for the doped BiOX compounds, the band structure of the D-doped BiOI is plotted in Figure 2a as an example (other BiOXs' are plotted in Figure S2). The semiconductor still keeps its indirect feature. The band gaps of the D-doped BiOI compounds are consistent with the pure model. However, an impurity level arises in gaps and influences the photoelectric property. For the Ag-doped

BiOI compounds, the impurity level is located in 0.006 eV, indicating that these kinds of compounds are p-type semiconductors. Similarly, the impurity level of the Pd-doped BiOI is at distance 1.437 eV from VBM and indicates a deep-level semiconductor.
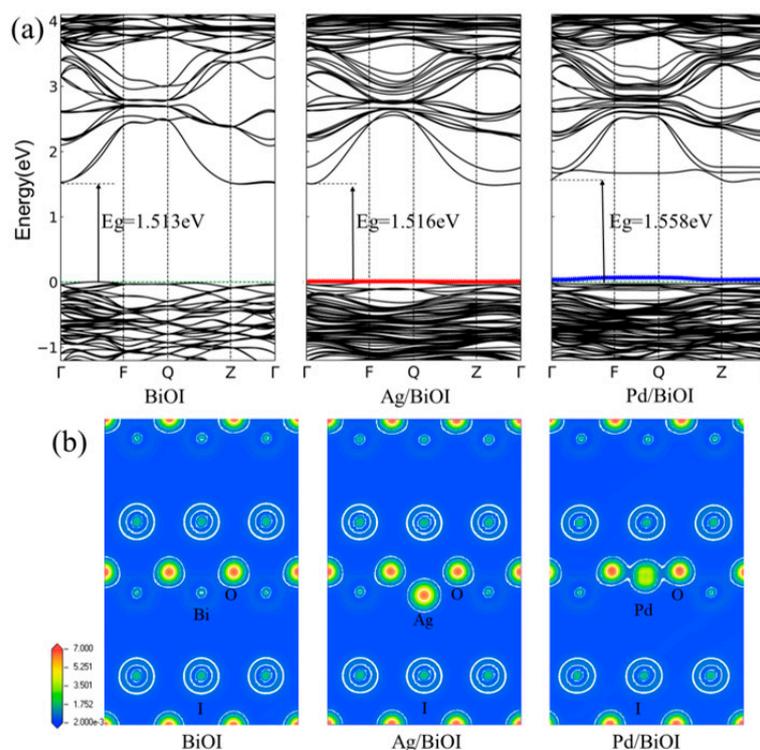

Figure 2. (**a**) The band structures of pure and D-doped BiOI and (**b**) their charge densities.

To further understand the behaviors in the D-doped BiOI models, the atomic populations and net charges were calculated via the Mulliken population analysis [45], and the results are shown in Table 2, and charge density pictures of the pure and D-doped BiOI structures are displayed in Figure 2b. From the Figure 2b, the charge density of D atoms in the doped BiOI compounds is larger than the Bi in the pure compounds because the net charge of the Bi atom in BiOI is 1.22 e while the net charge of the D (Ag and Pd) atoms are 0.1 and 0.13 e according to Table 2, respectively. Also, the density of Ag is higher than Pd, which indicates that the Pd covalent property is stronger than Ag. Furthermore, the population becomes bigger and the bond length d_i become smaller, which implies that the O-D bonds are stronger than the pure ones and present a certain covalent property.

Table 2. The net charge and bond population for pure and Ag-doped BiOI based on the Mulliken charge analysis. The locations of Oi-Bi, Oi-D are shown in Figure 1c.

BiOX	Net Charge/e				Population/e							
	Bi	O	X	D	O$_1$-Bi	O1-D	O2-Bi	O2-D	O3-Bi	O3-D	O4-Bi	O4-D
BiOI	1.22	−0.9	−0.32	-	0.11	-	0.11	-	0.11	-	0.11	-
Ag/BiOI	-	−0.84	−0.27	0.1	-	0.14	-	0.14	-	0.14	-	0.14
Pd/BiOI	-	−0.75	−0.27	0.13	-	0.32	-	0.32	-	0.32	-	0.32

Also, similar results also exist in the remaining D-doped BiOX (X = F, Cl, Br) compounds. The concrete data and figures are arranged in Table S2 and Figures S2 and S3. The impurity energy level could provide holes to the valence band and electrons to the conduction band. Therefore, the doped BiOX compounds will provide more photoexcited carriers and require less absorption energy than the undoped BiOX. Meanwhile, for the Pd-doped BiOX (X = F, Cl, Br), the band gap of the Pd-doped BiOX models are slightly smaller than the Ag-doped BiOX (X = F, Cl, Br), but a deeper level comes

up, which may influence the photocatalytic performance. As for the charge density, similar results are displayed. In summary, the doped atoms in the BiOX models contribute to the changes of the electronic distribution and the electronic features.

Therefore, the total and partial density of states (DOS) of the pure and D-doped BiOX were calculated, whose analyses of the contribution of the state have been discussed in previous works [17–20]. Now we will discuss the doped BiOX compounds. The DOS graphs are plotted in Figure 3.
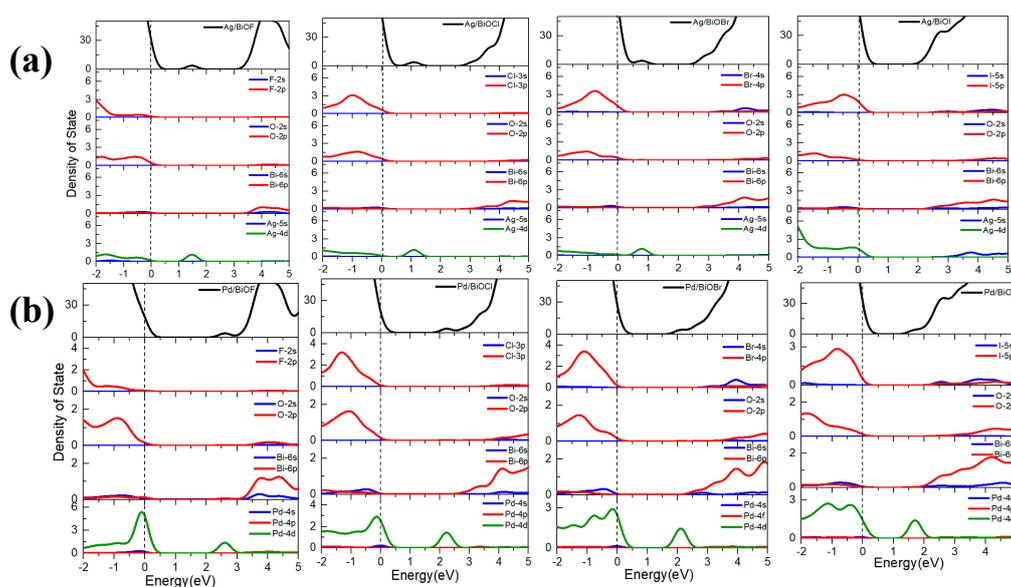

Figure 3. The density of state (DOS) of D-doped BiOX (X = F, Cl, Br, I). (**a**) The DOS of Ag-doped BiOX and (**b**) the DOS of Pd-doped BiOX.

For the Ag-doped BiOX models, it clearly indicates that the electronic structural features of the pure compounds remain intact except for the appearance of an impurity energy level, which originates from the Ag-4d state. This new state is located on the top of the valence band. The distances between the Ag impurity energy levels and VBMs are 1.391, 0.953, 0.717, and 0.006 eV for the Ag-doped BiOF, BiOCl, BiOBr, and BiOI models, respectively. The distance between impurity energy level and VBM decreases with the increase of halogen atomic numbers. The band gap of pure BiOF is largest one over all the BiOX compounds which indicates the greatest photon absorption energy and the worst light-harvesting ability. However, the dopant of Ag into the BiOF compound induces a deep energy level at 1.391 eV, implying that the impurity energy level probably acts as the recombination center of photogenerated charge carriers rather than the separation of electron-hole pairs [44]. The impurity energy level in the Ag-doped BiOCl and BiOBr compounds provides electrons to CBM and holes to VBM and is able to act as a springboard for electron transitions from the valence band to the conduction band by absorbing less photon energy. Moreover, the impurity energy level of the Ag-doped BiOBr and BiOCl compounds possesses appropriate depth compared to the excessive deep energy level of the Ag-doped BiOF. It is clearly speculated that the ability of photocatalytic activity may follow BiOBr > BiOCl > BiOI, which is in agreement with the previous experimental results [33]. Then, for the Pd-doped BiOX, similar properties are concluded by the DOS curving; the impurity energy level is from the Pd-4d state. All in all, the changes of the electronic structures would influence the optical absorption utilization factor to some degree, then affecting photocatalytic performance.

3.3. Optical Properties

The imaginary part ε_2 of the dielectric function is calculated in order to obtain absorption coefficients of pure and doped BiOX as a function of the energy of incident light and plotted in

Figure 4. The scissors operator, a grid upshift of CB to the experimental values, 1.2, 0.93, 0.62, and 0.36 eV for BiOF, BiOCl, BiOBr, and BiOI models respectively, was used to widen the band gap and obtain the corrected optical properties due to the underestimated band gap in this work. From Figure 4b,c, a strong peak between 0 and 10 eV is observed in the spectrum of pure BiOX (X = Cl, Br, I). It is assigned to the electronic transitions from VBM to the isolated low energy block in the conduction band. The peaks are centered at 6.028 eV for BiOCl, 5.381 eV for BiOBr, and 4.724 eV for BiOI respectively. For the BiOF compound from the Figure 4a, two peaks at 6.238 and 8.199 eV are observed. Those peaks are generated mainly by the transitions from O-2p and X-np states to Bi-6p and partially Bi-6s states. The peaks greater than 10 eV originated from the jumping of the O-2p and X-np states to the conduction bands of the upper levels. More importantly, the imaginary part of the dielectric function over Ag (Pd)-doped BiOX models shows a certain amount of red shift. According to Equations (1)–(3), absorption peaks show red shift at the range from 0 to ~4.370 eV contributing to the photocatalytic performance, which is due to the transition from Ag-4d states to conduction bands. The peak at 0.592 eV suggests that there is strong absorption near the infrared region. As for Pd-doped BiOX, certain enhancement of absorption peaks was observed in the visible region at the energy value lower than 4 eV. However, great changes occur on the Pd-doped BiOF compound, which is from the transition of Pd-4d states and the impurity energy level.
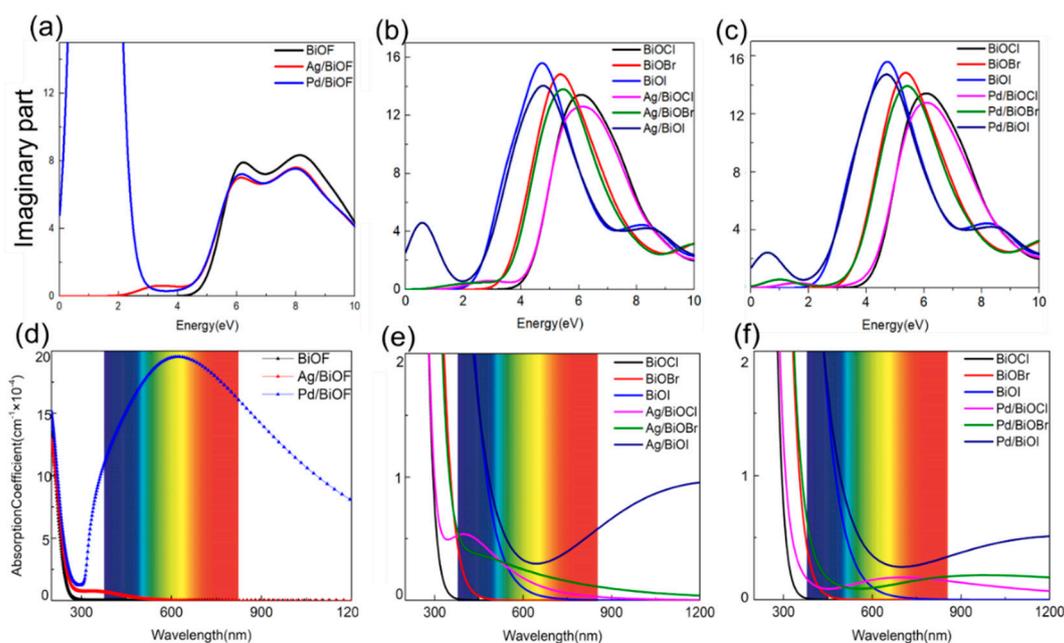

Figure 4. (**a**–**c**) The calculated imaginary part $\varepsilon 2$ of the dielectric constants and the unit in eV; (**d**–**f**) Absorption coefficients and unit in nm of the pure and doped BiOX (X = F, Cl, Br, I) as a function of the energy of incident light.

The absorption coefficients (in cm^{-1}) of the pure and D-doped BiOX are plotted in Figure 4d–f and absorption edges are recorded in Table 1. The absorption edges of pure BiOX models are 355, 451, and 650 nm for BiOCl, BiOBr, and BiOI models in accordance with experimental results at ~376, ~442, and ~628 nm, respectively [38]. The absorption edges of BiOX grow linearly with the atomic numbers of halogen. We also get the same result based on the early analysis of the imaginary part of the dielectric function. Remarkably, when the Ag impurity is doped, the absorption coefficients of Ag-doped BiOX models from 400–800 nm are larger than the pure BiOX. With regard to the Pd-doped BiOX model, the Pd-doped BiOCl and Pd-doped BiOBr show similar enhancement of absorption, but almost nothing has been changed for the Pd-doped BiOI compared to Ag-doped BiOX (X = Cl and Br). However, it is more interesting to see that the Pd-doped BiOF model shows a large difference from the other three compounds and that a high absorption coefficient located at the visible region even

the infrared light is observed. It can predict that the experimentally-prepared Pd-BiOF sample will present excellent photocatalytic properties based on our computation results, indicating the important progress in full spectrum catalysis.

4. Conclusions

In order to understand the photocatalytic mechanism of the D-doped BiOX compounds, especially the enhanced photocatalytic observed in the Ag-doped BiOX compound, the structural, electronic, and optical properties of Ag/Pd doped BiOX (X = F, Cl, Br, I) have been calculated based on the DFT used GGA-PBEsol. The Ag/Pd-doped structures keep the previous layered structures, which also assist in the separation of photoexcited carriers. As a result, the absorption coefficients become larger after doping, and the photocatalytic performances are enhanced further due to the changed electronic structures of the Ag/Pd doped BiOX compounds. The enhanced photocatalytic activity of the Ag-doped BiOI compounds is in line with the experimental results based on our DFT calculation of optoelectronic properties. Moreover, the photocatalytic efficiencies of the Ag-doped BiOCl and BiOBr compounds are higher than the one with the Pd-doped compound, which is also indicated by the better absorption under visible light in our calculation. Intriguingly, Pd-doped BiOF samples display unusual absorption peaks over the full spectrum wavelength according to the absorption spectrum, which may offer a significant strategy for one possible system with full-spectrum catalysis.

Supplementary Materials: The following are available online at http://www.mdpi.com/2073-4344/9/2/198/s1, Figure S1: The tested graphs of Ag-doped BiOBr model considering spin and $3 \times 3 \times 2$ k points. (a) The band structure and (b) the density of state. Figure S2: The band structures of pure and D-doped BiOX (D = Ag, Pd; X = F, Cl, Br). Figure S3: The charge density of pure and doped BiOX (101) (X = F, Cl, Br). Figure S4: The total and partial density of state of pure and D-doped BiOX (X = F, Cl, Br, I). Table S1: The variation of structural parameters plus the location of impurity level before and after doping. Table S2: The net charge and bond population for pure and D-doped BiOX.

Author Contributions: The manuscript was written through contributions of all authors. All authors have given approval to the final version of the manuscript.

Conflicts of Interest: The authors declare no conflict of interest.

References

1. Fujishima, A.; Honda, K. Electrochemical photolysis of water at a semiconducter electrode. *Nature* **1972**, *238*, 37–39. [CrossRef] [PubMed]
2. Sun, Y.; Sun, Z.; Gao, S.; Cheng, H.; Liu, Q.; Lei, F.; Wei, S.; Xie, Y. All-Surface-Atomic-Metal Chalcogenide Sheets for High-Efficiency Visible-Light Photoelectrochemical Water Splitting. *Adv. Energy Mater.* **2014**, *4*, 1300611. [CrossRef]
3. Weng, S.; Fang, Z.; Wang, Z.; Zheng, Z.; Feng, W.; Liu, P. Construction of teethlike homojunction BiOCl (001) nanosheets by selective etching and its high photocatalytic activity. *ACS Appl. Mater. Interfaces* **2014**, *6*, 18423–18428. [CrossRef] [PubMed]
4. Jin, X.; Ye, L.; Xie, H.; Chen, G. Bismuth-rich bismuth oxyhalides for environmental and energy photocatalysis. *Coord. Chem. Rev.* **2017**, *349*, 84–101. [CrossRef]
5. Di, J.; Xia, J.; Li, H.; Guo, S.; Dai, S. Bismuth oxyhalide layered materials for energy and environmental applications. *Nano Energy* **2017**, *41*, 172–192. [CrossRef]
6. Zhu, Z.; Huang, W.-R.; Chen, C.-Y.; Wu, R.-J. Preparation of Pd–Au/TiO_2–WO_3 to enhance photoreduction of CO_2 to CH_4 and CO. *J. CO_2 Util.* **2018**, *28*, 247–254. [CrossRef]
7. Ni, M.; Leung, M.K.H.; Leung, D.Y.C.; Sumathy, K. A review and recent developments in photocatalytic water-splitting using TiO_2 for hydrogen production. *Renew. Sustain. Energy Rev.* **2007**, *11*, 401–425. [CrossRef]

8.   Spadaro, L.; Arena, F.; Negro, P.; Palella, A. Sunfuels from CO_2 exhaust emissions: Insights into the role of photoreactor configuration by the study in laboratory and industrial environment. *J. CO2 Util.* **2018**, *26*, 445–453. [CrossRef]

9.   Zou, Z.; Ye, J.; Sayama, K.; Arakawa, H. Direct splitting of water under visible light irradiation with an oxide semiconductor photocatalyst. *Nature* **2001**, 625–627. [CrossRef]

10.   Yang, H.G.; Sun, C.H.; Qiao, S.Z.; Zou, J.; Liu, G.; Smith, S.C.; Cheng, H.M.; Lu, G.Q. Anatase TiO_2 single crystals with a large percentage of reactive facets. *Nature* **2008**, *453*, 638–641. [CrossRef] [PubMed]

11.   Kudo, A.; Miseki, Y. Heterogeneous photocatalyst materials for water splitting. *Chem. Soc. Rev.* **2009**, *38*, 253–278. [CrossRef] [PubMed]

12.   Liu, Y.; Son, W.J.; Lu, J.; Huang, B.; Dai, Y.; Whangbo, M.H. Composition dependence of the photocatalytic activities of $BiOCl_{1-x}Br_x$ solid solutions under visible light. *Chemistry* **2011**, *17*, 9342–9349. [CrossRef] [PubMed]

13.   Tong, H.; Ouyang, S.; Bi, Y.; Umezawa, N.; Oshikiri, M.; Ye, J. Nano-photocatalytic materials: Possibilities and challenges. *Adv. Mater.* **2012**, *24*, 229–251. [CrossRef] [PubMed]

14.   Liu, M.; Qiu, X.; Miyauchi, M.; Hashimoto, K. Energy-level matching of Fe(III) ions grafted at surface and doped in bulk for efficient visible-light photocatalysts. *J. Am. Chem. Soc.* **2013**, *135*, 10064–10072. [CrossRef] [PubMed]

15.   Zhang, K.; Liu, C.; Huang, F.; Zheng, C.; Wang, W. Study of the electronic structure and photocatalytic activity of the BiOCl photocatalyst. *Appl. Catal. B: Environ.* **2006**, *68*, 125–129. [CrossRef]

16.   Zhao, L.; Zhang, X.; Fan, C.; Liang, Z.; Han, P. First-principles study on the structural, electronic and optical properties of BiOX (X = Cl, Br, I) crystals. *Physica B* **2012**, *407*, 3364–3370. [CrossRef]

17.   Zhang, X.; Ai, Z.; Jia, F.; Zhang, L. Generalized One-Pot Synthesis, Characterization, and Photocatalytic Activity of Hierarchical BiOX ((X) Cl, Br, I) Nanoplate Microspheres. *J. Phys. Chem. C* **2008**, *112*, 747–753. [CrossRef]

18.   Huang, W.L.; Zhu, Q. Electronic structures of relaxed BiOX (X = F, Cl, Br, I) photocatalysts. *Comput. Mater. Sci.* **2008**, *43*, 1101–1108. [CrossRef]

19.   Huang, W.L.; Zhu, Q. Structural and electronic properties of BiOX (X = F, Cl, Br, I) considering Bi 5f states. *Comput. Mater. Sci.* **2009**, *46*, 1076–1084. [CrossRef]

20.   Wu, S.; Wu, D. First principle calculations of photocatalytic properties of bismuth oxyhalides considering van der Waals correction. In Proceedings of the IEEE International Conference on EIT, Grand Forks, ND, USA, 19–21 May 2016; pp. 452–457. [CrossRef]

21.   Zhang, L.; Tang, Z.K.; Lau, W.M.; Yin, W.J.; Hu, S.X.; Liu, L.M. Tuning band gaps and optical absorption of BiOCl through doping and strain: Insight form DFT calculations. *Phys. Chem. Chem. Phys.* **2017**, *19*, 20968–20973. [CrossRef]

22.   Zhang, W.; Zhang, Q.; Dong, F. Visible-Light Photocatalytic Removal of NO in Air over BiOX (X = Cl, Br, I) Single-Crystal Nanoplates Prepared at Room Temperature. *Ind. Eng. Chem. Res.* **2013**, *52*, 6740–6746. [CrossRef]

23.   Liu, G.; Wang, T.; Ouyang, S.; Liu, L.; Jiang, H.; Yu, Q.; Kako, T.; Ye, J. Band-structure-controlled $BiO(ClBr)_{(1-x)/2}I_x$ solid solutions for visible-light photocatalysis. *J. Mater. Chem. A* **2015**, *3*, 8123–8132. [CrossRef]

24.   Kong, L.; Jiang, Z.; Lai, H.H.; Nicholls, R.J.; Xiao, T.; Jones, M.O.; Edwards, P.P. Unusual reactivity of visible-light-responsive AgBr–BiOBr heterojunction photocatalysts. *J. Catal.* **2012**, *293*, 116–125. [CrossRef]

25.   Tang, Z.K.; Yin, W.J.; Le, Z.; Wen, B.; Zhang, D.Y.; Liu, L.M.; Lau, W.M. Spatial separation of photo-generated electron-hole pairs in BiOBr/BiOI bilayer to facilitate water splitting. *Sci. Rep.* **2016**, *6*, 32764. [CrossRef] [PubMed]

26.   Dai, G.; Yu, J.; Liu, G. Synthesis and Enhanced Visible-Light Photoelectrocatalytic Activity. *J. Phys. Chem. C* **2011**, *115*, 7339–7346. [CrossRef]

27.   Chai, S.Y.; Kim, Y.J.; Jung, M.H.; Chakraborty, A.K.; Jung, D.; Lee, W.I. Heterojunctioned $BiOCl/Bi_2O_3$, a new visible light photocatalyst. *J. Catal.* **2009**, *262*, 144–149. [CrossRef]

28.   Ye, L.; Zan, L.; Tian, L.; Peng, T.; Zhang, J. The {001} facets-dependent high photoactivity of BiOCl nanosheets. *Chem. Commun.* **2011**, *47*, 6951–6953. [CrossRef]

29. Zhang, X.; Li, B.; Wang, J.; Yuan, Y.; Zhang, Q.; Gao, Z.; Liu, L.M.; Chen, L. The stabilities and electronic structures of single-layer bismuth oxyhalides for photocatalytic water splitting. *Phys. Chem. Chem. Phys.* **2014**, *16*, 25854–25861. [CrossRef]

30. Zhao, Z.Y.; Dai, W.W. Structural, electronic, and optical properties of Eu-doped BiOX (X = F, Cl, Br, I): A DFT+U study. *Inorg. Chem.* **2014**, *53*, 13001–13011. [CrossRef]

31. Zhao, Z.Y.; Liu, Q.L.; Dai, W.W. Structural, Electronic, and Optical Properties of $BiOX_{1-x}Y_x$ (X, Y = F, Cl, Br, and I) Solid Solutions from DFT Calculations. *Sci. Rep.* **2016**, *6*, 31449. [CrossRef]

32. Yu, C.L.; Cao, F.F.; Shu, Q.; Bao, Y.L.; Xie, Z.P.; Yu, J.; Yang, K. Preparation, Characterization and Photocatalytic Performance of AgBiOX (X = Cl, Br, I) Composite Photocatalysts. *Acta Phys. Chim. Sin.* **2012**. [CrossRef]

33. Yu, C.; Cao, F.; Li, G.; Wei, R.; Yu, J.C.; Jin, R.; Fan, Q.; Wang, C. Novel noble metal (Rh, Pd, Pt)/BiOX(Cl, Br, I) composite photocatalysts with enhanced photocatalytic performance in dye degradation. *Sep. Purif. Technol.* **2013**, *120*, 110–122. [CrossRef]

34. Ye, L.; Liu, J.; Gong, C.; Tian, L.; Peng, T.; Zan, L. Two Different Roles of Metallic Ag on Ag/AgX/BiOX (X = Cl, Br) Visible Light Photocatalysts: Surface Plasmon Resonance and Z-Scheme Bridge. *ACS Catal.* **2012**, *2*, 1677–1683. [CrossRef]

35. Chen, F.; Huang, H.; Zeng, C.; Du, X.; Zhang, Y. Achieving Enhanced UV and Visible Light Photocatalytic Activity for Ternary Ag/AgBr/BiOIO₃: Decomposition for Diverse Industrial Contaminants with Distinct Mechanisms and Complete Mineralization Ability. *ACS Sustain. Chem. Eng.* **2017**, *5*, 7777–7791. [CrossRef]

36. Kim, W.J.; Pradhan, D.; Min, B.-K.; Sohn, Y. Adsorption/photocatalytic activity and fundamental natures of BiOCl and $BiOCl_xI_{1-x}$ prepared in water and ethylene glycol environments, and Ag and Au-doping effects. *Appl. Catal. B: Environ.* **2014**, *147*, 711–725. [CrossRef]

37. Wyckoff, R. Design of p-type transparent conducting oxides Sn_2GeO_4 by an ab initio evolutionary structure search. *J. Mater. Chem. C* **2018**. [CrossRef]

38. An, H.; Du, Y.; Wang, T.; Wang, C.; Hao, W.; Zhang, J. Photocatalytic properties of BiOX (X = Cl, Br, and I). *Rare Met.* **2008**, *27*, 243–250. [CrossRef]

39. Segall, M.D.; Lindan, P.J.D.; Probert, M.J.; Pickard, C.J.; Hasnip, P.; Clark, S.J.; Payne, M.C. First-principles simulation ideas, illustrations and the CASTEP code. *IOPscience* **2002**, 2717–2744. [CrossRef]

40. Perdew, J.P.; Ruzsinszky, A.; Csonka, G.I.; Vydrov, O.A.; Scuseria, G.E.; Constantin, L.A.; Zhou, X.; Burke, K. Restoring the density-gradient expansion for exchange in solids and surfaces. *Phys. Rev. Lett.* **2008**, *100*, 136406. [CrossRef]

41. Monkhorst, H.J.; Pack, J.D.; Freeman, D.L. Lithium crystal properties from high-quality Hartree-Fock wave functions. *Solid State Commun.* **1979**, *29*, 723–725. [CrossRef]

42. Shanno, D.F.; Phua, K.-H. Matrix conditioning and nonlinear optimization. *Math. Program.* **1978**, *14*, 149–160. [CrossRef]

43. Gajdoš, M.; Hummer, K.; Kresse, G.; Furthmüller, J.; Bechstedt, F. Linear optical properties in the projector-augmented wave methodology. *Phys. Rev. B* **2006**, *73*. [CrossRef]

44. Van de Walle, C.G.; Neugebauer, J. First-principles calculations for defects and impurities: Applications to III-nitrides. *J. Appl. Phys.* **2004**, *95*, 3851–3879. [CrossRef]

45. Mulliken, R.S. Electronic Population Analysis on LCAO–MO Molecular Wave Functions. *J. Chem. Phys.* **1955**, *23*, 1833–1840. [CrossRef]